Multi-scale structures of electric current generated by collisionless trapped electron mode turbulence

Xiang Chen[1],Zhixin Lu[2,a],Huishan Cai[1,b],Lei Ye[3],Yang Chen[4],Ding Li[5,6,7],Jian Liu[1,9] and Zhaoyuan Liu[8,9]

[1]School of Nuclear Science and Technology, University of Science and Technology of China, Hefei 230026, China
[2]Max Planck Institut für Plasmaphysik, Garching, Germany
[3]Institute of Plasma Physics, Chinese Academy of Sciences, Hefei 230031, China
[4]Center for Integrated Plasma Studies, University of Colorado at Boulder, Boulder, CO 80309, United States
[5]Institute of Physics, Chinese Academy of Sciences, Beijing 100190, China
[6]Songshan Lake Materials Laboratory, Dongguan, Guangdong 523808, China
[7]University of Chinese Academy of Sciences, Beijing 100049, China
[8]Shandong Computer Science Center (National Supercomputing Center in Jinan), Qilu University of Technology (Shandong Academy of Sciences) , Jinan, Shandong, 250014, China
[9]Advanced Algorithm Joint Lab, Shandong Computer Science Center, Qilu University of Technology, Jinan, Shandong 250014, China

E-mail: zhixin.lu@ipp.mpg.de,hscai@mail.ustc.edu.cn

Abstract. The spatial structure and amplitude of the current induced by the collisionless trapped electron mode (CTEM) turbulence are investigated by the gyrokinetic simulations. It is shown that the barely passing electrons play a crucial role in determining the magnitude and the direction of the current density. Two characteristic radial scales of the current density are found. The fine structure (a few ion Larmor radii) of the turbulence-induced current is observed near the rational surfaces. Further, the mesoscale structure (tens of ion Larmor radii) of the turbulence-induced current related to the zonal flow shear is confirmed, especially for the high toroidal mode number (n) CTEM. For the strongly driven CTEM, the zonal flow shear effect on the turbulence-induced current is significant, while it is not visible for the weakly driven CTEM. The magnitude of the CTEM turbulence-induced current density is featured with moderate local magnitude comparable to the bootstrap current density near the rational surfaces, which is shown by the nonlinear simulations with multi-n modes.

1. Introduction

The researches of the past decades have shown that the drift waves are the prominent candidates for the radial transport of particles, energy, and momentum in the magnetic fusion devices. Because of the large ion-to-electron mass ratio, the momentum transport of ions and electrons have different effects on plasma confinement. The self-driven toroidal rotation in tokamak has been intensively researched, which is related to the turbulence induced ion momentum transport [1, 2, 3]. The intrinsic rotation can be induced by the symmetry breaking of the turbulence spectrum, due to specific mechanisms, such as the turbulence intensity gradient [4], profiles shearing [5], zonal flow shear [2], and the radial shift of the poloidal harmonics [6]. Even though the electron momentum transport has negligible impacts on the plasma rotation, it significantly affects the spontaneous plasma current in tokamak [7, 8, 9, 10, 11, 12, 13].

This self-induced current by turbulence modifies the current density profiles [12] and affects magnetohydrodynamic(MHD) instabilities. It provides interpretation of MHD activities due to turbulence effects [14, 15]. S. I. Itoh and K. Itoh have demonstrated this current firstly with a slab model [7]. McDevitt has analyzed three mechanisms of the turbulence-induced current, namely, (1) the electron residual stress, which redistributes the electron momentum, (2) the turbulence acceleration, which changes the total momentum of electrons, and (3) the turbulence induced resonant electron scattering, which is similar to the mechanism of bootstrap current [16, 17]. Further analyses by Wang [12] have suggested that the turbulence intensity gradient and the zonal flow shear make the dominant contributions on the symmetry breaking. The symmetry breaking is needed for the generation of the residual stress and the turbulence acceleration. Our previous studies [13] have demonstrated the fine structure of the current generated by the ion temperature gradient turbulence. However, the effects of the zonal flow shear on current generation are not clear when the fine structure current is generated.

In this work, two cases with different parameters are performed with the GEM code [18, 19] to demonstrate the effects of the zonal flow on the turbulence-induced current in CTEM turbulence [20, 21, 22]. Two scale structures of current density are identified by the continuous wavelet transform (CWT) method. One is the fine current structure near the rational surface caused by the resonance between the turbulence and the fast moving electrons [13]. The other is the mesoscale structure of current density which is closely connected to the zonal flow shear. The amplitude of the current density is evaluated by multi-n simulations.

The remainder of this paper is organized as follows. In Sec. 2, the gyrokinetic simulation tool and parameters are introduced in detail. In Sec. 3, the zonal flow effects on turbulence-induced current are detailed and the amplitude of the current density is obtained by multi-n simulations. Finally, the paper is concluded in Sec. 4.

2. Gyrokinetic simulation model and parameters

2.1. Simulation model

This work is performed using the GEM [18, 19] code, which solves the gyrokinetic Poisson-Ampére equations with the gyrokinetic ions and the drift-kinetic electrons. In the 5D phase space, GEM solves the perturbed distribution function δf based on the Particle-in-Cell (PIC) method. In this method, δf is sampled by the marker particles and the split-weight scheme is implemented. The perturbed electric field ($\delta\phi$) and the perturbed parallel vector potential $\left(A_{\|}\right)$ are solved on spatial grids while the marker particles are evolved step by step providing the distribution in Lagrangian frame [23]. For the perturbed field, $\delta\phi$ is calculated by solving the Poisson equation valid for arbitrary wavelength [24] and $A_{\|}$ is calculated according to the Ampère's equation. In the electromagnetic gyrokinetic formulation, the canonical momentum $p_{\|} = v_{\|} + q/mA_{\|}$ is adopted to solve the numerical difficulty caused by $\partial A_{\|}/\partial t$. However, it introduces a large current term in the Ampère's equation. This non-physical current should be cancelled, otherwise it will lead to inaccuracy as well as the numerical instability. Many efforts have been spent on the treatment of this cancellation problem such as the mixed variable/pullback scheme [25, 26] and the implicit scheme [27]. In GEM, an iterative scheme has been developed to mitigate the cancellation problem successfully in the $p_{\|}$ formula [19].

2.2. Parameters relevant to the simulations and basic linear properties

In the following simulations, the concentric circular magnetic equilibrium with the DIII-D Cyclone Base Case (CBC) [28] geometry is adopted, $R_0 = 1.67\mathrm{m}, a/R_0 = 0.36$, where a and R_0 are the minor and major radius respectively. The realistic ion-electron mass ratio $m_\mathrm{i}/m_\mathrm{e} = 3672$ is considered and deuterium is the only ion species. The safety factor profile is $q(r) = 2.52(r/a)^2 - 0.16r/a + 0.84$, and the magnetic shear is defined as $\hat{s} = d\mathrm{ln}q/d\mathrm{ln}r$. The equilibrium density and temperature profiles, denoted as $H(r)$, and the normalized logarithmic gradients R_0/L_H, are given by [29, 13]

$$\frac{H(r)}{H(r_0)} = \exp\left[-\kappa_\mathrm{H} w_\mathrm{H} \frac{a}{R_0} \tanh\left(\frac{r - r_0}{w_\mathrm{H} a}\right)\right] \quad , \tag{1}$$

$$\frac{R_0}{L_\mathrm{H}} = -R_0 \frac{d\ln H(r)}{dr} = \kappa_\mathrm{H} \cosh^{-2}\left(\frac{r - r_0}{w_\mathrm{H} a}\right) \quad , \tag{2}$$

where $L_\mathrm{H} = -\left[d\ln H(r)/dr\right]^{-1}$ is the characteristic length of profile $H(r)$, and $r_0 = a/2$. To eliminate the ITG instabilities, cold ions ($T_\mathrm{e}/T_\mathrm{i} = 3$) are chosen [30] and the characteristic length of density profile and ion temperature profile are $R_0/L_\mathrm{n} = 3.33$ and $R_0/L_\mathrm{Ti} = 2.22$ respectively. Two cases are performed and compared with $R_0/L_\mathrm{Te} = 5$ and 10 respectively. There are two dimensionless parameters. One is $\beta_\mathrm{e} = n_\mathrm{e} T_\mathrm{e}/(B_0^2/2\pi\mu_0) = 0.01\%$ which is defined by the electron density, temperature at r_0 and the magnetic field on axis ($B_0 = 2.0\mathrm{T}$). The other is $\rho^* = \rho_\mathrm{s}/a \sim 1/312$ which denotes the ratio of ion gyroradius and minor radius. It should be noted that the Coulomb collision effects are not considered in this work.

The growth rate and frequency as a function of wavenumber (n) are shown in Fig. 1, where the blue line represents the case with $R_0/L_\mathrm{Te} = 5$ and the yellow line denotes the case with $R_0/L_\mathrm{Te} = 10$. The growth rate and frequency are calculated near $r/a = 0.5$ where the gradient of temperature and density are greater and the modes are more unstable. As shown in the left panel of Fig. 1, the growth rate of the yellow line is much higher than the blue line. The case with $R_0/L_{\mathrm{Te}} = 10$ is more unstable than the case with $R_0/L_{\mathrm{Te}} = 5$ due to its strong electron temperature gradient. In this work, two cases with $R_0/L_{\mathrm{Te}} = 5$ and $R_0/L_{\mathrm{Te}} = 10$ are denoted as the weakly driven case and the strongly driven case, respectively. The CTEM is confirmed according to the real frequency shown in the right panel of Fig. 1 since negative frequencies indicate modes propagating in the electron diamagnetic drift direction.

3. The simulation results of the CTEM induced current

In this section, the results of the CTEM induced current are demonstrated. It is known that the zonal flow shear plays an important role on the turbulence mitigation [31, 32], the intrinsic rotation of bulk ions [2], and the current generation [12]. In our simulations, two cases with the different electron temperature gradient ($R_0/L_{\mathrm{Te}} = 5, 10$) are performed to take into account the zonal flow shearing effects on the current generation and its connection with the fine structure of the current density [13]. In this work, the global simulations are performed with the fixed boundary condition and the numerical parameters are as follows: The simulation box size is $1/n$th torus with the radial length $l_x = 0.7a$ ($218\rho_i$). The grid resolution is $n_x \times n_y \times n_z = 512 \times 32 \times 64$, where n_x and n_z are the grids points number in the radial diretion and the parallel direction, respectively. The number of ions and electrons per cell are $N_i = 32$ and $N_e = 48$, respectively. Time step is $\omega_{ci}\Delta t = 2$, where ω_{ci} is the ion gyrofrequency.

3.1. The characteristics of perturbed electron distribution function corresponding to current generation

Even though several physical mechanisms of the turbulence-induced current have been proposed, the characteristics of perturbed electron distribution function corresponding to the turbulence-induced current have not been discussed individually in detail for CTEM when the fine structure of current is taken into account. To illustrate how electrons contribute to the turbulence-induced current, nonlinear simulations with a single CTEM ($n = 20$) and zonal mode ($n = 0$) are performed in the strongly driven case. In the turbulence saturation stage, the perturbed distribution of the electron parallel velocity ($v_\parallel \delta f_e$) is sampled in a small box on the low field side of the mid-plane ($\theta = 0$) in tokamak geometry. The parallel electric current induced by turbulence is defined as $\mathrm{j_{\parallel,tur}} = -\mathrm{e}\int \mathrm{d^3 v v_\parallel \delta f_e}$ and its magnitude and direction are determined by the perturbed electron distribution (δf_e). The positive $\mathrm{j_{\parallel,tur}}$ denotes the cocurrent direction. There is no turbulence-induced current if $v_\parallel \delta f_e$ is anti-symmetric with respect to $v_\parallel$ (i.e., δf_e is symmetric with respect to $v_\parallel$).

The structures of $v_\parallel \delta f_e$ on the box between two neighboring rational surfaces ($q = 27/20$ and $q = 28/20$) and near the rational surface ($q = 28/20$) are shown in the left panel and right panel of Fig. 2, respectively. Six signed peaks from different electron groups are located alternately in the $(v_\parallel, v_\perp)$ space and the red straight lines represent the boundaries between the trapped and passing electrons. The perturbed distribution of the electron parallel velocity ($h = v_\parallel \delta f_e$) is decomposed into the even parity component $h_{\mathrm{even}} = [h(v_\parallel) + h(-v_\parallel)]/2$ and the odd parity component $h_{\rm odd} = [h(v_\parallel) - h(-v_\parallel)]/2$, and the odd parity component has no contribution to the current generation. Although the trapped particles carry significant amount of $v_\parallel \delta f_e$, the odd parity component of $v_\parallel \delta f_e$ is dominant and cancelled each other a large part. Only the even parity component of $v_\parallel \delta f_e$ leads to the net current generation.

In order to identify the contributions of trapped and passing electrons to the current generation, further analyses are performed in Fig. 3 with $v_\parallel \delta f_e$ along $v_\parallel$ at $v_\perp = 0.75 v_{\rm th}$ (bottom left panel), $v_\perp = 1.75 v_{\rm th}$ (middle left panel), and $v_\perp = 2.75 v_{\rm th}$ (top left panel), where $v_{th} \equiv \sqrt{T_e/m_e}$ is the electron thermal velocity. The blue and red lines denote $v_\parallel \delta f_e$ on the box between two rational surfaces ($q = 27/20$ and $q = 28/20$) and near the rational surface ($q = 28/20$) respectively. The vertical dash lines are the boundaries between the trapped and passing electrons. In the top left panel of Fig. 3, $v_\parallel \delta f_e$ is mainly carried by the trapped electrons and the odd parity component of $v_\parallel \delta f_e$ is dominant. Therefore, the net current carried by the electrons with $v_\perp \sim 2.75 v_{\rm th}$ is negligible. In the mid and bottom left panels of Fig. 3, besides the cancelled current carried by the trapped electrons, the net current is mainly carried by the barely passing electrons. There is a negative net current and positive net current between two rational surfaces and near the rational surface as shown by the blue and red lines, respectively. In the right panel of Fig. 3, the current density is negative and positive between two rational surfaces (the regime between the red dash lines) and near the rational surface (the regime between the black dash line), which is consistent with the results shown in the left panel of Fig. 3. Thus, it is concluded that the barely passing electrons play a key role in the current generation in determining the magnitude and direction of the current density.

3.2. Nonlinear properties of the weakly and strongly driven CTEM

The poloidal harmonics of CTEM are centered on their respective rational surface at $r_{m,n}$, where $q(r_{m,n}) = m/n$ and m is the poloidal mode number. The width of the harmonics is comparable to several times of the distance between two neighbouring rational surfaces $\Delta r = 1/nq'$. Since the zonal flow has more significant effects on high n modes, the nonlinear simulations with the single CTEM ($n = 100$) and zonal mode ($n = 0$) are performed to investigate the zonal flow effects on turbulence-induced current. The turbulence time evolution and the spatio-temporal $\Omega_{\rm s}$ of the weakly and strongly driven cases are presented in Fig 4. The zonal flow shearing rate is $\Omega_{\rm s} = \partial v_{\boldsymbol{E}\times\boldsymbol{B},\theta}/\partial r$, where $v_{\boldsymbol{E}\times\boldsymbol{B},\theta} = -\hat{\boldsymbol{\theta}} \cdot \nabla \delta\phi_{\rm ZF} \times \boldsymbol{B}/B^2$, $\hat{\boldsymbol{\theta}}$ is the unit vector in poloidal direction and $\delta\phi_{\rm ZF}$ denotes the zonal potential. As shown in Fig. 4(a) and 4(b), the turbulence intensity I increases exponentially in the linear stage and reaches saturation in the nonlinear stage. In addition, the stronger drive leads to the higher saturation level. The interaction between zonal flow and the drift wave turbulence is described theoretically as the predator-prey model [33]. On one hand, the zonal component of the electric potential $\delta\phi_{\rm ZF}$ increases with the intensity of CTEM. On the other hand, it breaks the CTEM eddies and reduces the turbulence saturation level. Thus, with the higher turbulence saturation level, the zonal flow shear Ω_s for the strongly driven case is much higher than that for the weakly driven case as shown in Fig. 4(c) and 4(d). For the strongly driven case, $\Omega_{\rm s}/\Omega \sim 2-4$ while for the weakly driven case $\Omega_{\rm s}/\Omega \ll 1$. When the zonal flow shearing rate is a few times larger than the mode frequency Ω, the zonal flow shear has significant stabilization effects on the drift waves [34]. In the next section, these two cases are analyzed to identify the zonal flow effects on the turbulence-induced current.

3.3. The zonal flow effects on the multi-scale structures of turbulence-induced current

The time-averaged turbulence intensity and the induced current over the turbulence saturated stage are shown in Fig. 5. For the weakly driven case with $\Omega_{\mathrm{s}}/\Omega \ll 1$, the zonal flow has negligible effects on the turbulence and the turbulence-induced current as shown in Fig. 5(a) and 5(c). Since the fine structure of turbulence intensity is absent, it is indicated that the fine structure of the current density near the rational surface results from the electron transit resonance with CTEM within a very narrow electron Landau layer. For the strongly driven case with $\Omega_{\mathrm{s}}/\Omega \sim 2-4$, the zonal flow breaks up the turbulence eddies and provides an additional symmetry breaking mechanism which drives the current. Both the turbulence and its induced current have the mesoscale structure related to the zonal flow [32] as shown in Fig. 5(b) and 5(d).

The detailed spatial scale analyses of the zonal flow and turbulence-induced current are shown in Fig. 6. To separate the multiple scales of physical quantities along the radial direction, the CWT method is adopted. Compared with the Fourier transform which cannot handle both slow and fast signals simultaneously, the CWT method has the advantage in the analyses of the non-stationary signal. It is defined as follows

$$F(l,\tau) = \frac{1}{\sqrt{|\tau|}} \int f(x)\psi\left(\frac{x-l}{\tau}\right) dx, \tag{3}$$

where $f(x)$ is the signal to be analyzed and $\psi\left[(x-l)/s\right]$ is the transformed signal or the wavelet function. l is the translation parameter which is related to the location of the wavelet and τ is the scale parameter which is related to the width of the wavelet. A series of wavelet functions with different scales are multiplied by the signal and then integrated over all domain. In this work, the analytic Morse wavelet [35] is adopted. The fine structure current generation is closely connected to the structure of the turbulence intensity and the wave-electron resonance condition. The meso-scal current structure is related to the zonal flow which provides a $k_{\parallel}$ symmetry breaking mechanism and produces the electron residual stress[2]. Since it is the divergence of the residual stress that drives the electron parallel flow, the wavelet transform of $\partial\Omega_{\mathrm{s}}/\partial r$ and $j_{\parallel,\mathrm{tur}}$ are compared to demonstrate the zonal flow shear effects on turbulence current generation. The transformed results of $\partial\Omega_{\mathrm{s}}/\partial r$ and $\mathrm{j}_{\parallel,\mathrm{tur}}$ in the nonlinear stage for the weakly and strongly driven cases are shown in Fig. 6. The red lines in Fig. 6(b) and 6(d) denote the inverse of the width between two neighbouring rational surfaces ($k_{\mathrm{r}} = 2\pi nq'$). The bright pattern of the CWT results of $\mathrm{j}_{\parallel,\mathrm{tur}}$ aligns with the red line and $k_{\mathrm{r}}a \sim 250$ ($k_{\mathrm{r}}\rho_{\mathrm{s}} \sim 0.8$) as shown in Fig. 6(b). It is demonstrated that the radial scale of current density is close to the width between two neighboring rational surfaces. However, as shown in Fig. 6(a), the radial structure scale of $\partial\Omega_{\mathrm{s}}/\partial r$ is $k_{\mathrm{r}}a \sim 50$ ($k_{\mathrm{r}}\rho_{\mathrm{s}} \sim 0.16$) which is about 5 times width of the current density radial structures scale. Therefore, in the weakly driven case, the effects of the zonal flow shear on the turbulence-induced current are negligible. It is indicated that the current is mainly induced by the electron-wave resonance near the rational surface [13] and the symmetry breaking of the turbulence intensity gradient [4, 12]. While for the strongly driven case, besides the fine structure distributed along the red line, the turbulence-induced current has a wider radial scale, featured with the spectrum $k_{\mathrm{r}}a \sim 30$ ($k_{\mathrm{r}}\rho_{\mathrm{s}} \sim 0.1$) as shown in Fig. 6 (d). Clearly, the characteristic structure of $k_{\mathrm{r}}a \sim 30$ ($k_{\mathrm{r}}\rho_{\mathrm{s}} \sim 0.1$) is observed in both $\partial\Omega_{\mathrm{s}}/\partial r$ and current density profiles in 6(c) and 6(d). Besides the fine structure of current density near the rational surface, the mesoscale structure of current density produced by the zonal flow shear is indicated by the CWT method. It is indicated that zonal flow shear with small structure (with high k_r) in radial direction can drive meso-scale parallel current more efficiently since the divergence of the residual stress drives the current.

In this work, the arbitrary wavelength field solver is adopted so that the fine structure of turbulence can also be included in the simulation. Furthermore, with the CWT method, two structures of turbulence induced current are separated for the strongly driven case in the CBC parameter regime. One is the fine structure of current density which is caused by the electron-wave resonance near the rational surface and the symmetry breaking induced by the turbulence intensity gradient [4, 13]. The other is the mesoscale structure of current density which is related to the symmetry breaking induced by the zonal flow shear[2, 12].

3.4. Multiple n simulations of the CTEM turbulence induced current

In this section, in order to identify the overall effects of zonal flow shear on the current density, multi-n simulations including $n = 0, 5, 10, \ldots, 100$ in the strongly driven case are performed. The mode spectra in Fourier space, turbulence intensity and the current density profiles in the linear and nonlinear stages are shown in Fig. 7. In the linear stage, the turbulence intensity profile is shown in Fig. 7(c) and the most unstable mode $n = 50$ is dominant as shown in Fig. 7(a). In Fig. 7(e), the CTEM induced current has spike structures near the rational surface which arise from the symmetry breaking mechanisms and wave-particle resonance. In the nonlinear stage, the frequency spectrum indicates that the amplitude of ITG is much smaller than the amplitude of CTEM ($\sim 20\%$ of the amplitude of CTEM). In Fig. 7(b), the low n modes near $n = 15$ are dominant in the nonlinear stage due to the inverse cascading to the low n modes and the higher saturation level of the low n modes. Even though the zonal flow shear provides a symmetry breaking mechanism and produces the mesoscale structure of current density, its effects on the current generation for low n turbulence are not as visible as shown in Sec. 3.3. In Fig. 7(d) and Fig. 7(f), it is clearly demonstrated that turbulence intensity and the turbulence-induced current has spike structures near the rational surfaces $q = 6/5(r/a = 0.402)$ and $q = 7/5(r/a = 0.496)$ for the 1/5th torus simulations. Because at these exact resonance surfaces, the resonant harmonics have much bigger net contribution to the turbulence intensity and turbulence-induced current[13].

the mesoscale structure of current density is less visible due to the dominance of the fine structures. From the observation in Fig. 6, it is shown by the high n simulation more clearly that the structures with the scale $k_{\mathrm{r}}a \sim 30$ ($k_{\mathrm{r}}\rho_{\mathrm{s}} \sim 0.1$) appear in both $\partial\Omega_{\mathrm{s}}/\partial r$ and $\mathrm{j}_{\parallel,\mathrm{tur}}$. However, in the multiple n nonlinear simulations, the low n modes are dominant in the nonlinear stage. Consequently, on one hand, the scale of the $\mathrm{j}_{\parallel,\mathrm{tur}}$ structure along the $k_{\mathrm{r}}a \sim a/(nq')$ shifts towards the scale of $\partial\Omega_{\mathrm{s}}/\partial r$. On the other hand, high n modes and the associated mesoscale structures of $\mathrm{j}_{\parallel,\mathrm{tur}}$ are less dominant.

The wavelet transform method is adopted to separate the different scale structures of the turbulence-induced current and the zonal flow shearing rate in the multi-n simulations. In Fig. 8,

$\partial\Omega_s/\partial r$ (left panel) has the structure $k_r a \sim 55$ ($k_r\rho_s \sim 0.18$) between $r/a = 0.3$ and $r/a = 0.4$ and the current density (right panel) also has the similar structure near $r/a = 0.4$. Moreover, the turbulence-induced current has the structures between two rational surface as shown in the right panel of Fig. 8 where the upper and bottom red line are $k_r = 2\pi nq'$ for $n = 10$ and $n = 5$, respectively. Because the width between two rational surfaces of low n approaches to the mesoscale structure of the zonal flow, the fine scale structure and mesoscale structure of the current density merge together. The resulting $j_{\|,tur}$ pattern can be affected by the synergy of the zonal flow shearing in the plasma and the symmetry breaking mechanism near the rational mode surfaces.

It is computationally expensive to perform a full n simulation of CTEM turbulence induced current. As shown in the previous work [13], $\Delta n = 5$ is appropriate to predict the amplitude of the turbulence-induced current, where $\Delta n = 5$ corresponds to the one fifth torus simulation including $n = 0, 5, 10, \ldots, n_{max}$. For the strongly driven case, the maximum toroidal mode number is $n_{\max} = 100$. The grid resolution is $n_x \times n_y \times n_z = 512 \times 384 \times 56$. The electron and ion numbers per cell are $N_e = 32$ and $N_i = 24$, respectively. The time averaged turbulence-induced current is presented in Fig. 9, where the blue curve is the turbulence-induced current and the black curve is the bootstrap current. It is shown that the turbulence-induced current density is about 50% of the bootstrap current density in magnitude especially near the low n rational surface. It corrugates the current density significantly and may affect the MHD instabilities, such as the neoclassical tearing mode (NTM)[14].

4. Conclusions

In this work, the current induced by the collisionless trapped electron mode has been studied using the gyrokinetic code GEM. The main results of this work are summarized as follows.

(i) It is demonstrated by the electron phase space structure analyses that the barely passing electrons play a key role in the current generation in determining the magnitude and direction of current density. The even parity component of the current phase space structure along $v_\|$ direction leads to the net current.

(ii) Two characteristic radial scales of the current density are separated by the wavelet transform method. One is the fine structure (a few ion Larmor radii) which is induced by the electron-wave resonance near the rational surface and the symmetry breaking of the turbulence intensity. The other is the mesoscale structure (tens of ion Larmor radii) which is related to the zonal flow shear.

(iii) For the weakly driven CTEM case, the induced current is dominated by the fine structures near the rational mode surfaces and the zonal flow has negligible effects on current generation. For the strongly driven CTEM case, the zonal flow shear regulates the current generation significantly for high n modes, while for low n modes, the fine structure of current density near the rational mode surfaces is dominant.

(iv) For the multi-n nonlinear simulations of the strongly drive case, the current density structure is determined by the synergistic effects of zonal flow shear in the plasma (related to the mesoscale structure) and the symmetry breaking near rational mode surfaces (related to the fine scale structure).

(v) It is shown by the nonlinear simulations that the CTEM tubulence-induced current density is about 50% as the bootstrap current density in magnitude for the strongly driven CTEM case near the rational surfaces.

In this work, we focused on the identification of the multi-scale structure of the CTEM induced current and the effects of the zonal flow shear on the structure and amplitude of current density. Studies using realistic experimental parameters and the effects of various parameters on the current density magnitude can be done in the future. Beside the CTEM in the electrostatic limit, the electromagnetic effects or the electromagnetic modes such as kinetic ballooning mode and β induced Alfvén eigenmode, may bring in different physical phenomena of the turbulence current drive and will be studied in the future. Furthermore, the turbulence may induce current with fine structure and mesoscale structure inside a magnetic island, and may impact on NTM dynamics indirectly. It merits more efforts to identify the effects of the turbulence-induced current on the onset threshold and behavior of NTM in order to control the NTM and improve the confinement in future experiments.

Acknowledgments

This work is supported by the National Natural Science Foundation of China (Grant Nos. 11822505, 11835016, and 11675257), the Youth Innovation Promotion Association CAS, the Users with Excellence Program of Hefei Science Center CAS (Grant No. 2019HSC-UE013), the Fundamental Research Funds for the Central Universities (Grant No. WK3420000008), and the Collaborative Innovation Program of Hefei Science Center CAS (Grant No. 2019HSC-CIP014). The numerical calculations in this paper were performed on the Hefei advanced computing center.

The data that support the findings of this study are available from the corresponding author upon reasonable request.

[1] Rice J E, Duval B P, Reinke M L, Podpaly Y A, Bortolon A, Churchill R M, Cziegler I, Diamond P H, Dominguez A, Ennever P C, Fiore C L, Granetz R S, Greenwald M J, Hubbard A E, Hughes J W, Irby J H, Ma Y, Marmar E S, McDermott R M, Porkolab M, Tsujii N and Wolfe S M 2011 *Nucl. Fusion* **51** 083005

[2] Wang W X, Hahm T S, Ethier S, Rewoldt G, Lee W W, Tang W M, Kaye S M and Diamond P H 2009 *Phys. Rev. Lett.* **102**(3) 035005

[3] Diamond P H, Kosuga Y, Gürcan O D, McDevitt C J, Hahm T S, Fedorczak N, Rice J E, Wang W X, Ku S, Kwon J M, Dif-Pradalier G, Abiteboul J, Wang L, Ko W H, Shi Y J, Ida K, Solomon W, Jhang H, Kim S S, Yi S, Ko S H, Sarazin Y, Singh R and Chang C S 2013 *Nucl. Fusion* **53** 104019

[4] Gürcan O D, Diamond P H, Hennequin P, McDevitt C J, Garbet X and Bourdelle C 2010 *Phys. Plasmas* **17** 112309

[5] Camenen Y, Idomura Y, Jolliet S and Peeters A G 2011 *Nucl. Fusion* **51** 073039

[6] Lu Z, Wang W X, Diamond P H, Tynan G, Ethier S, Chen J, Gao C and Rice J E 2015 *Nucl. Fusion* **55** 093012

[7] Itoh S I and Itoh K 1988 *Phys. Lett. A* **127** 267–269 ISSN 0375-9601

[8] Hinton F L, Waltz R E and Candy J 2004 *Phys. Plasmas* **11** 2433–2440

[9] Wang W W, Ethier S, Hahm T, Tang W, Boozer A *et al.* 2012 Turbulence generated non-inductive current and flow shear driven turbulent transport in tokamaks *24th Int. Conf. on Fusion Energy (San Diego, 2012),TH/P7-14*

[10] Garbet X, Esteve D, Sarazin Y, Dif-Pradalier G, Ghendrih P, Grandgirard V, Latu G and Smolyakov A 2014 *J. Phys.: Conf. Ser.* **561** 012007

[11] He W, Wang L, Peng S T, Guo W X and Zhuang G 2018 *Nucl. Fusion* **58** 106004

[12] Wang W X, Hahm T S, Startsev E A, Ethier S, Chen J, Yoo M G and Ma C H 2019 *Nucl. Fusion* **59** 084002

[13] Chen X, Lu Z, Cai H, Ye L, Chen Y and Gao B 2021 *Phys. Plasmas* **28** 112303

[14] Cai H S 2018 *Nucl. Fusion* **59** 026009

[15] Li E, Zou X L, Xu L Q, Chu Y Q, Feng X, Lian H, Liu H Q, Liu A D, Han M K, Dong J Q, Wang H H, Liu J W, Zang Q, Wang S X, Zhou T F, Huang Y H, Hu L Q, Zhou C, Qu H X, Chen Y, Lin S Y, Zhang B, Qian J P, Hu J S, Xu G S, Chen J L, Lu K, Liu F K, Song Y T, Li J G and Gong X Z (EAST Team) 2022 *Phys. Rev. Lett.* **128**(8) 085003

[16] Bickrton R J, Connor J W and Taylor J B 1971 *Nat. Phys. Sci.* **229** 110–112

[17] Peeters A G 2000 *Plasma Phys. Controlled Fusion* **42** B231–B242

[18] Chen Y and Parker S E 2003 *J. Comput. Phys.* **189** 463–475 ISSN 0021-9991

[19] Chen Y and Parker S E 2007 *J. Comput. Phys.* **220** 839–855

[20] Rosenbluth M and Sloan M L 1971 *The Physics of Fluids* **14** 1725–1741

[21] Coppi B and Rewoldt G 1974 *Phys. Rev. Lett.* **33** 1329–1332

[22] Catto P J and Tsang K T 1978 *The Physics of Fluids* **21** 1381–1388

[23] Garbet X, Idomura Y, Villard L and Watanabe T 2010 *Nuclear Fusion* **50** 043002

[24] Dominski J, McMillan B F, Brunner S, Merlo G, Tran T M and Villard L 2017 *Phys. Plasmas* **24** 022308

[25] Hatzky R, Kleiber R, Könies A, Mishchenko A, Borchardt M, Bottino A and Sonnendrcker E 2019 *Journal of Plasma Physics* **85** 905850112

[26] Mishchenko A, Könies A, Kleiber R and Cole M 2014 *Phys. Plasmas* **21** 092110

[27] Lu Z, Meng G, Hoelzl M and Lauber P 2021 *J. Comput. Phys.* **440** 110384

[28] Dimits A M, Bateman G, Beer M A, Cohen B I, Dorland W, Hammett G W, Kim C, Kinsey J E, Kotschenreuther M, Kritz A H, Lao L L, Mandrekas J, Nevins W M, Parker S E, Redd A J, Shumaker D E, Sydora R and Weiland J 2000 *Phys. Plasmas* **7** 969–983

[29] Görler T, Tronko N, Hornsby W A, Bottino A, Kleiber R, Norscini C, Grandgirard V, Jenko F and Sonnendrcker E 2016 *Phys. Plasmas* **23** 072503

[30] Lang J, Chen Y and Parker S E 2007 *Phys. Plasmas* **14** 082315

[31] Hahm T S and Burrell K H 1995 *Phys. Plasmas* **2** 1648–1651

[32] Xiao Y and Lin Z 2009 *Phys. Rev. Lett.* **103**(8) 085004

[33] Diamond P H, Itoh S I, Itoh K and Hahm T S 2005 *Plasma Phys. Controlled Fusion* **47** R35–R161

[34] Hahm T S, Beer M A, Lin Z, Hammett G W, Lee W W and Tang W M 1999 *Phys. Plasmas* **6** 922–926

[35] Olhede S and Walden A 2002 *IEEE Transactions on Signal Processing* **50** 2661–2670

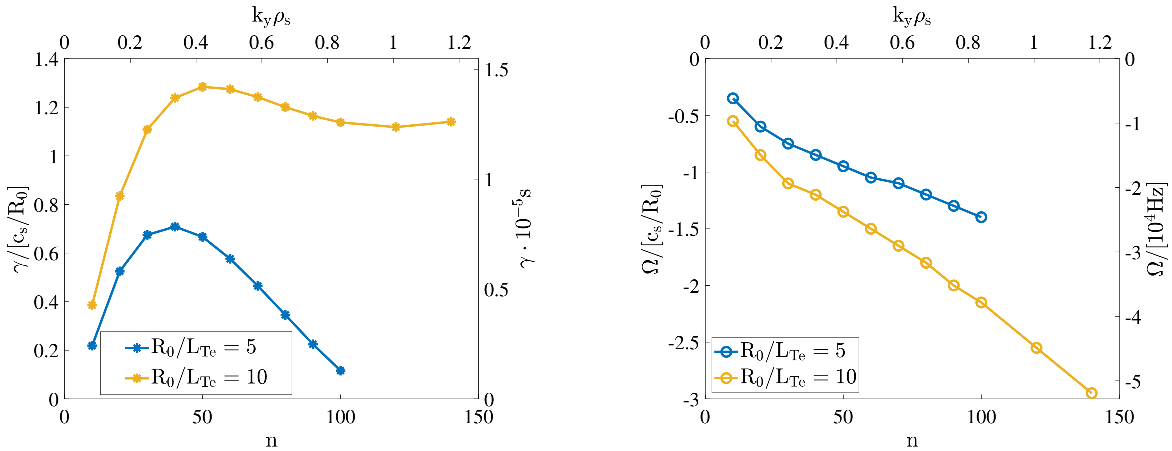

Figure 1. The growth rate (left panel) and frequency(right panel) for the cases with $R_0/L_{\mathrm{Te}} = 5$ and 10. The negative frequency direction is along the electron diamagnetic drift direction.

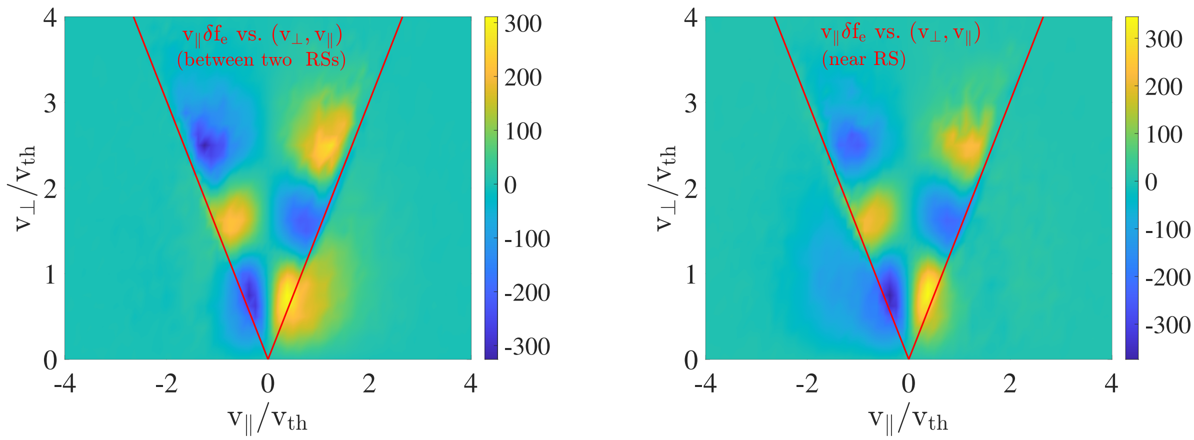

Figure 2. The perturbed distribution of the electron parallel velocity ($v_\parallel \delta f_e$) in the turbulence saturation stage. The left panel denotes the $v_\parallel \delta f_e$ sampled on the box between two neighboring rational surfaces ($q = 27/20$ and $q = 28/20$) and the right panel denotes that near the rational surface ($q = 28/20$). The red straight lines represent the boundaries between the trapped and passing electrons.

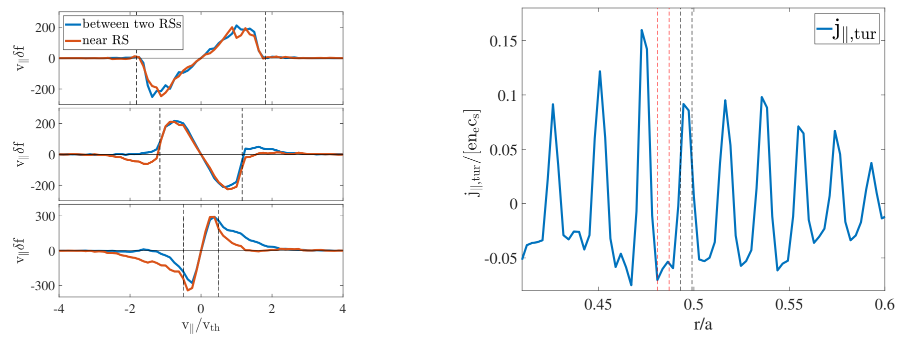

Figure 3. $v_{\|}\delta f_e$ versus $v_{\|}$ at $v_{\perp} = 0.75v_{\rm th}$ (bottom left panel), $v_{\perp} = 1.75v_{\rm th}$ (mid left panel) and $v_{\perp} = 2.75v_{\rm th}$ (top left panel). The blue line of the left panel denotes $v_{\|}\delta f_e$ sampled in the box between two neighboring rational surfaces ($q = 27/20$ and $q = 28/20$), the red line denotes that near the rational surface ($q = 28/20$) and the vertical dash lines represent the boundaries between the trapped and passing electrons. The right panel is the radial profile of the turbulence-induced current and the vertical red dash lines are the region between two rational surfaces ($q = 27/20$ and $q = 28/20$) and the vertical black dash lines are the region near the rational surface ($q = 28/20$).

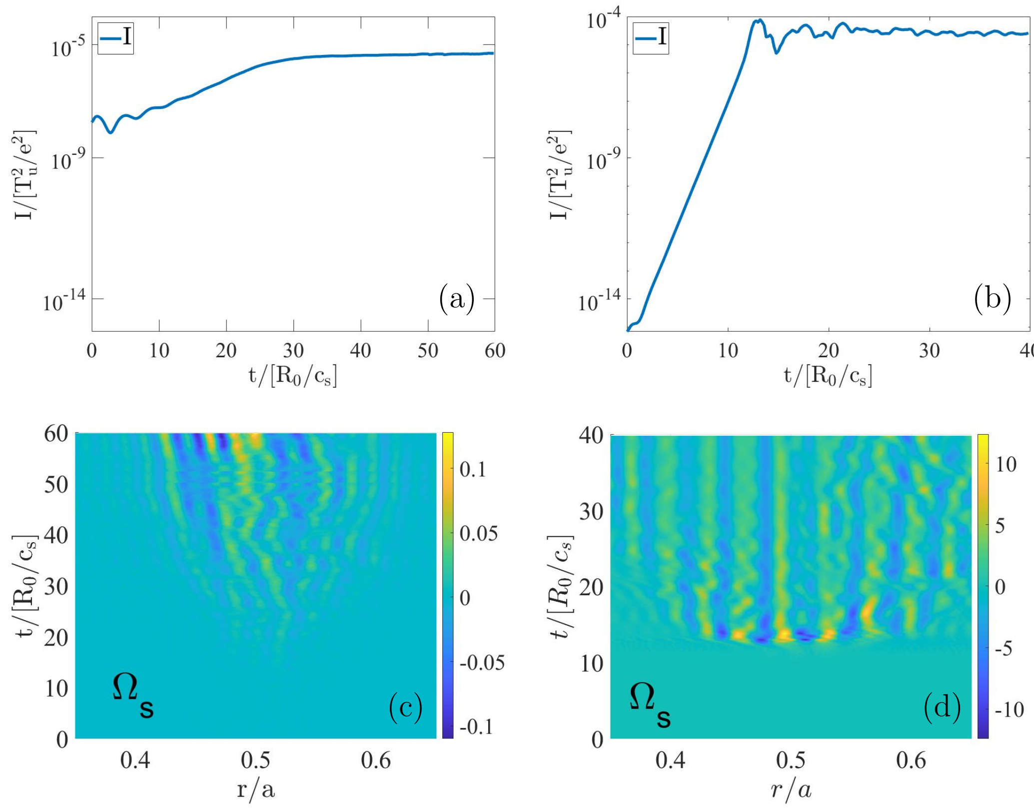

Figure 4. Turbulence time evolution with $R_0/L_{\rm Te} = 5$ (a) and $R_0/L_{\rm Te} = 10$ (b). The spatial and temporal evolution of zonal flow shearing rate $\Omega_{\rm s}/[c_{\rm s}/R_0]$ with $R_0/L_{\rm Te} = 5$ (c) and $R_0/L_{\rm Te} = 10$ (d).

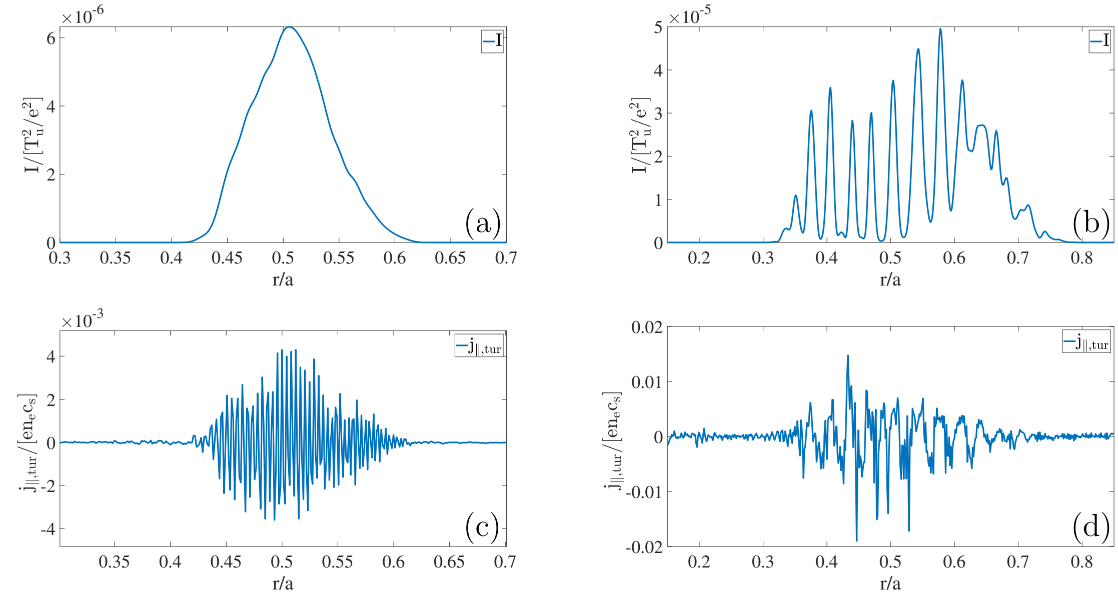

Figure 5. Time-averaged turbulence intensity in the saturation stage with $R_0/L_{\rm Te} = 5$ (a) and $R_0/L_{\rm Te} = 10$ (b). Time-averaged turbulence-induced current in the saturation stage with $R_0/L_{\rm Te} = 5$ (c) and $R_0/L_{\rm Te} = 10$ (d).

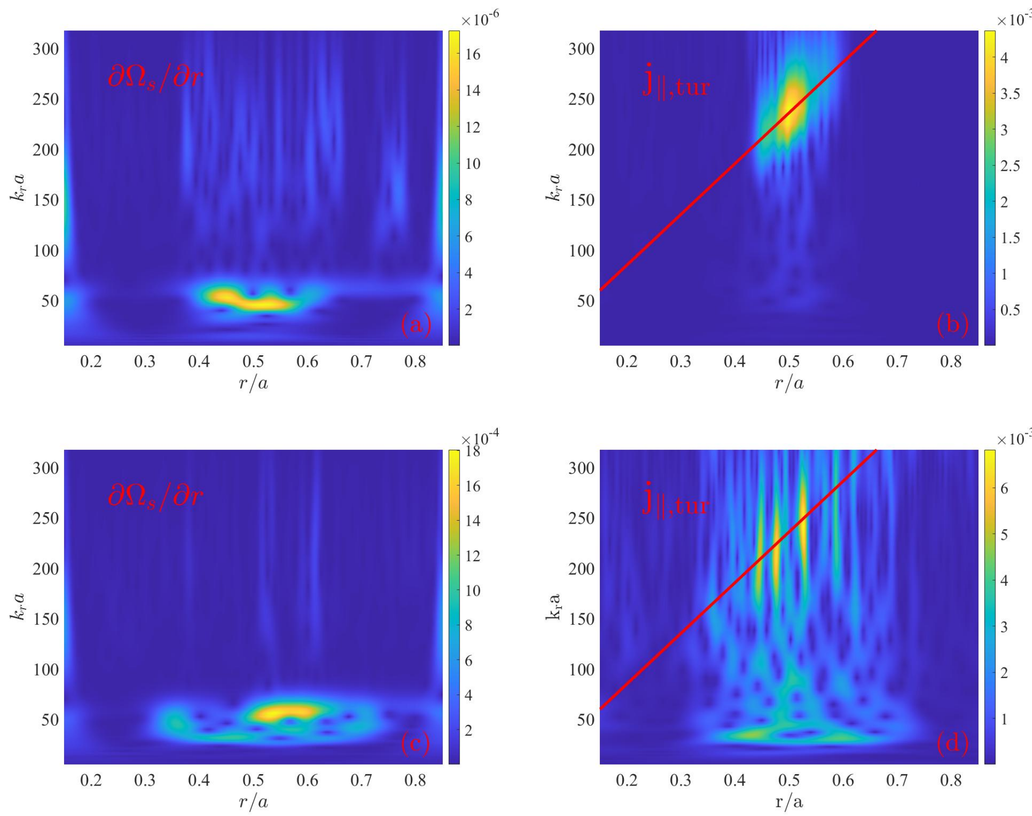

Figure 6. Wavelet transform of $\partial\Omega_{\rm s}/\partial r$ with $R_0/L_{\rm Te} = 5$ (a) and $R_0/L_{\rm Te} = 10$ (c). Wavelet transform of turbulence-induced current with $R_0/L_{\rm Te} = 5$ (b) and $R_0/L_{\rm Te} = 10$ (d).

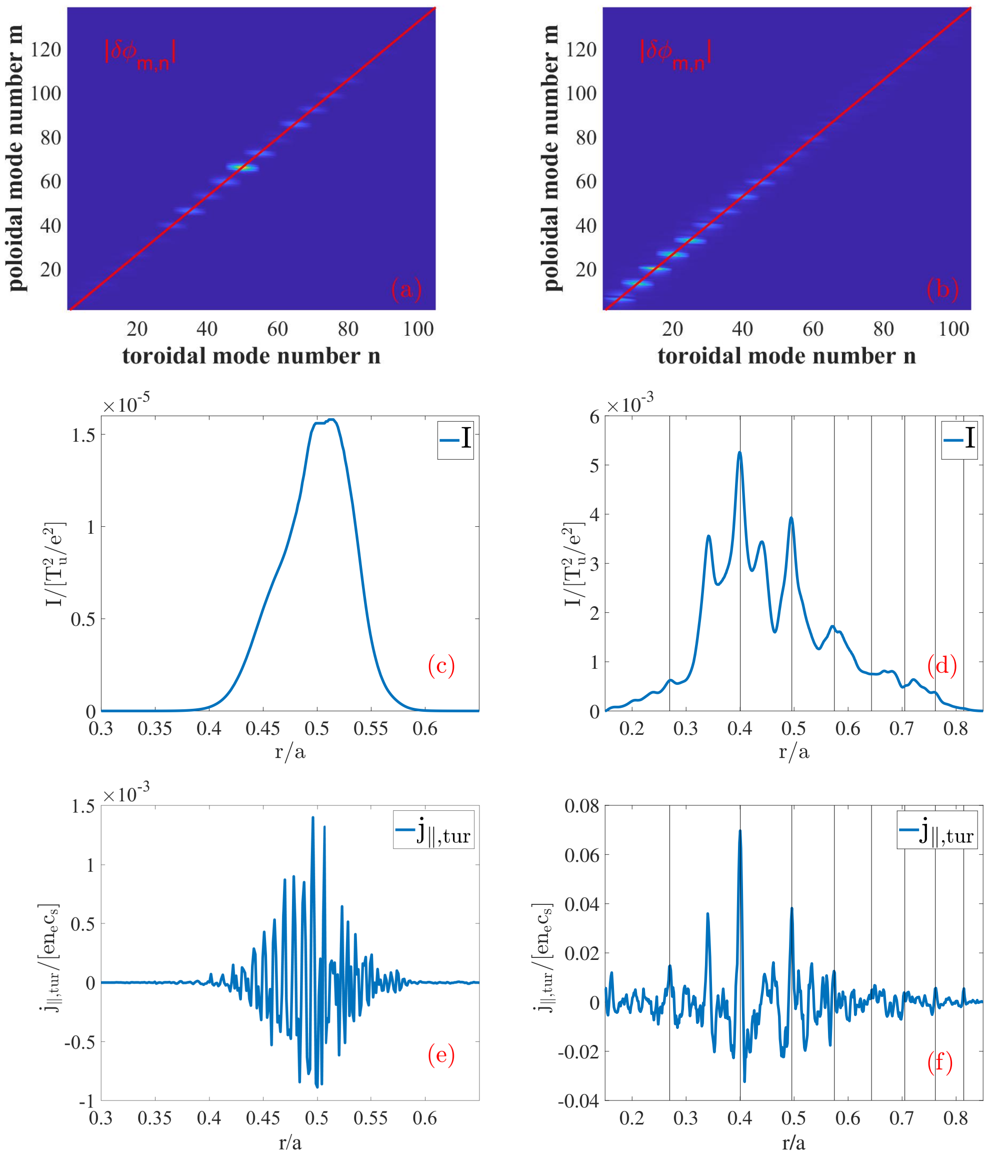

Figure 7. Mode decomposition in linear (a) and nonlinear stage (b). Turbulence intensity in linear (c) and nonlinear stage (d). CTEM induced current in the linear (e) and nonlinear stage (f).

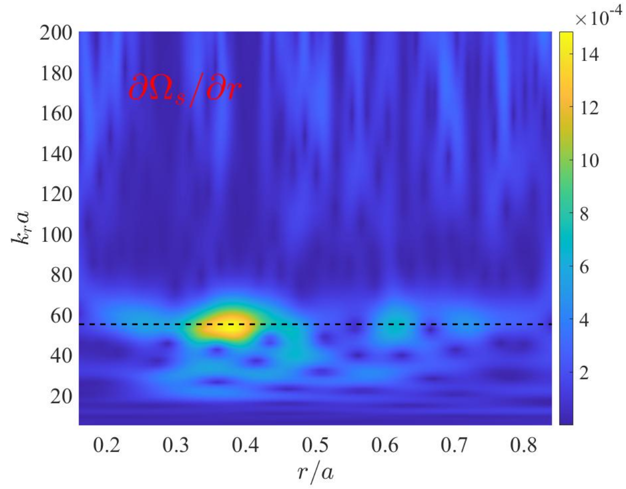

Figure 8. Wavelet transform of $\partial\Omega_{\mathrm{s}}/\partial r$ (left panel) and turbulence-induced current (right panel) in the nonlinear stage. The horizontal dash lines denote $k_{\mathrm{r}}a = 55$. The upper and bottom red lines are $k_{\mathrm{r}} = 2\pi n q'$ for $n = 10$ and $n = 5$, respectively.

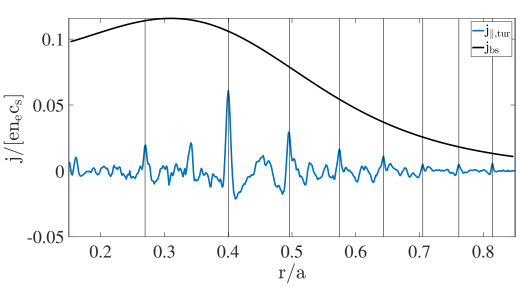

Figure 9. turbulence-induced current (blue line) and bootstrap current (black line), $\Delta n = 5$ means that the multi-n simulations only include $n = 0, 5, \ldots, 100$. The vertical black lines are the rational surfaces of $n = 5$.